

# AN ALMA SURVEY OF FAINT DISKS IN THE CHAMAELEON I STAR-FORMING REGION: WHY ARE SOME CLASS II DISKS SO FAINT?

FENG LONG(龙凤),<sup>1,2</sup> GREGORY J. HERCZEG(沈雷歌),<sup>1</sup> ILARIA PASCUCCI,<sup>3,4</sup> DANIEL APAI,<sup>3,4,5</sup> THOMAS HENNING,<sup>6</sup>  
CARLO F. MANARA,<sup>7</sup> GIJS D. MULDER,<sup>3,4</sup> LÁSZLÓ. SZŰCS,<sup>8</sup> AND NATHANIAL P. HENDLER<sup>3</sup>

<sup>1</sup>*Kavli Institute for Astronomy and Astrophysics, Peking University, Beijing 100871, China*

<sup>2</sup>*Department of Astronomy, School of Physics, Peking University, Beijing 100871, China*

<sup>3</sup>*Lunar and Planetary Laboratory, University of Arizona, Tucson, AZ 85721, USA*

<sup>4</sup>*Earths in Other Solar Systems Team, NASA Nexus for Exoplanet System Science*

<sup>5</sup>*Steward Observatory, University of Arizona, Tucson, AZ 85721, USA*

<sup>6</sup>*Max Planck Institute for Astronomy, Heidelberg, Germany*

<sup>7</sup>*European Southern Observatory, Karl-Schwarzschild-Str. 2, D-85748 Garching bei München, Germany*

<sup>8</sup>*Max-Planck-Institut für extraterrestrische Physik, Giessenbachstrasse 1, D-85748 Garching, Germany*

## ABSTRACT

ALMA surveys of nearby star-forming regions have shown that the dust mass in the disk is correlated with the stellar mass, but with a large scatter. This scatter could indicate either different evolutionary paths of disks or different initial conditions within a single cluster. We present ALMA Cycle 3 follow-up observations for 14 Class II disks that were low S/N detections or non-detections in our Cycle 2 survey of the  $\sim 2$  Myr-old Chamaeleon I star-forming region. With 5 times better sensitivity, we detect millimeter dust continuum emission from six more sources and increase the detection rate to 94% (51/54) for Chamaeleon I disks around stars earlier than M3. The stellar-disk mass scaling relation reported in [Pascucci et al. \(2016\)](#) is confirmed with these updated measurements. Faint outliers in the  $F_{mm}-M_*$  plane include three non-detections (CHXR71, CHXR30A, and T54) with dust mass upper limits of  $0.2 M_{\oplus}$  and three very faint disks (CHXR20, ISO91, and T51) with dust masses  $\sim 0.5 M_{\oplus}$ . By investigating the SED morphology, accretion property and stellar multiplicity, we suggest for the three millimeter non-detections that tidal interaction by a close companion ( $\lesssim 100$  AU) and internal photoevaporation may play a role in hastening the overall disk evolution. The presence of a disk around only the secondary star in a binary system may explain the observed stellar SEDs and low disk masses for some systems.

*Keywords:* ALMA, protoplanetary disks, binary, disk evolution

## 1. INTRODUCTION

Protoplanetary disks orbiting young stars are the birthplaces of planetary systems. The lifetimes of disks set strong constraints on the timescale for giant planet formation. The disk frequency, as estimated from near- and mid-IR excess emission and the presence of accretion, declines with age, leading to a typical disk lifetime of  $\sim 3 - 5$  Myr (e.g. Haisch et al. 2001; Hernández et al. 2007; Fedele et al. 2010). ALMA surveys of nearby star-forming regions show a declining trend of average dust disk mass with cluster age, for the set of stars that retain disks (e.g., Ansdell et al. 2016, 2017; Barenfeld et al. 2016; Pascucci et al. 2016). Within any young cluster, the dust mass in the disk is correlated with the stellar mass, but with a large scatter. Some disks are detected in the mid-IR but are undetected in the sub-mm. This scatter indicates that disks within a single cluster evolve differently, with a possible dependence on initial conditions (Mulders et al. 2017; Lodato et al. 2017), stellar multiplicity (e.g., Harris et al. 2012), or other stellar or environmental properties. The transition from primordial to debris disks is still uncertain (Moór et al. 2017), but may be traced either by disks that are very faint in the sub-mm (e.g. Hardy et al. 2015; Espaillat et al. 2017) or by disks with inner cavities (e.g., Kim et al. 2009; Merín et al. 2010; Ercolano & Pascucci 2017).

Protoplanetary disks are physically and chemically complex systems that evolve through an interplay of different mechanisms. Current proposed disk evolution and/or dissipation mechanisms include viscous accretion (Hartmann et al. 1998), photoevaporation (Clarke et al. 2001; Owen et al. 2012; Alexander et al. 2014), dust grain growth and settling (Dullemond & Dominik 2005), as well as dynamical sculpting by planets formed within (Lissauer & Stevenson 2007; Durisen et al. 2007; Zhu et al. 2012; Pinilla et al. 2015). These mechanisms affect disk evolution around individual low-mass stars. Since about half of stars are in multiple systems (see review by Duchêne & Kraus 2013),

stellar multiplicity adds another important factor altering the evolution of any circumstellar or circumbinary disk in a multiple system (Papaloizou & Pringle 1977; Artymowicz & Lubow 1994; Miranda & Lai 2015; Lubow et al. 2015).

In a previous ALMA 887  $\mu\text{m}$  survey, we characterized the scaling relation between dust disk mass ( $M_{\text{dust}}$ ) and stellar mass ( $M_{\star}$ ) for low-mass stars in the 2–3 Myr-old Chamaeleon I star-forming region (Pascucci et al. 2016), located at an average distance of 190 pc<sup>1</sup>. The continuum emission was detected from  $\sim 80\%$  of disks around stars with spectral type earlier than M3 (the *Hot* sample) and  $\sim 55\%$  of disks around stars with later spectral type (the *Cool* sample). The non-detections have low dust masses and may have undergone faster/different disk evolution or perhaps be in a transitional stage between primordial and debris disks.

In this paper, we present results from a follow-up ALMA survey of 887  $\mu\text{m}$  continuum emission for the 14 faintest disks in the *Hot* sample of Pascucci et al. (2016), including the 9 non-detections in the *Hot* sample. We describe this follow-up survey in Section 2, present results from this survey and describe the anomalously faint sources in Section 3 and 4, and finally discuss the potential explanations for these faint sources as well as the implications of these results in Section 5.

## 2. OBSERVATIONS AND DATA REDUCTION

In our ALMA Cycle 2 program 2013.1.00437 (PI: I. Pascucci), a sample of 93 protoplanetary disks (complete down to M6) in Chamaeleon I was observed in Band 7 (Pascucci et al. 2016). The disks were selected based on the presence of excess mid-IR emission and prior classification as a

<sup>1</sup> For this paper, we adopt an updated average distance for Chamaeleon I of  $\sim 190$  pc, based on an analysis of Gaia DR2 parallaxes (Gaia Collaboration et al. 2018). This distance is consistent with the Gaia DR1 distance of 188 pc (Long et al. 2017, see also Voirin et al. 2017) but larger than the pre-Gaia distance of 160 pc adopted by Pascucci et al. (2016).

**Table 1.** ALMA Cycle 3 Observations

UTC Date	Antenna	Baseline Range	pwv	Calibrators		
	Number	(m)	(mm)	Flux	Bandpass	Phase
2016 Jan 25	42	15-331	1.13	J1107-4449	J1427-4206	J1058-8003
2016 Mar 30	44	15-460	0.75	J1107-4449	J1427-4206	J1058-8003

NOTE—All targets were observed on both nights.

Class II object by [Luhman et al. \(2008\)](#). The targets in this survey were split into a *Hot* sample with shallow observations, and a *Cool* sample with observations that were 5 times deeper. The block of stars in the *Hot* sample was observed to a sensitivity of 1 mJy/beam and delivered prior to the Cycle 3 deadline, so we were able to request deeper observations of the faintest *Hot* stars in our Cycle 3 program 2015.1.00333 (PI: I. Pascucci). The name and spectral type for each of these sources are listed in Table 2.

The ALMA Band 7 observational setup in Cycle 3 was similar to that in Cycle 2 (see the details of numbers of 12m antennas, baseline range, weather condition and calibrators listed in Table 1). The three continuum basebands were centered at 333.8, 335.7, and 347.5 GHz with an aggregated bandwidth of 5.9 GHz and a weighting-averaged frequency of 340 GHz ( $882 \mu\text{m}$ )<sup>2</sup>. The spectral line window was set to target  $^{12}\text{CO } J = 3 - 2$ , instead of the  $^{13}\text{CO}$  and  $\text{C}^{18}\text{O } J = 3 - 2$  lines targeted in Cycle 2, because the CO isotopologue emission is very faint and usually undetected ([Long et al. 2017](#)). For each source, two sets of observations were executed for a total integration time of 3.6 min, reaching a  $1\sigma$  rms of  $0.2 \text{ mJy beam}^{-1}$ , compared to  $\sim 1.0 \text{ mJy}$  for the *Hot* sample in our Cycle 2 data ([Pascucci et al. 2016](#)).

<sup>2</sup> The observed wavelength is slightly different from  $887 \mu\text{m}$  in [Pascucci et al. \(2016\)](#), leading to a flux difference expected to be  $< 1\%$ . In this paper, we use  $887 \mu\text{m}$  when referring to the millimeter continuum band for consistency.

The data calibration was performed using CASA 4.6.0, following the scripts provided by NRAO, including flux, phase, bandpass, and gain calibrations. We used J1427-4206 for bandpass calibration and J1058-8003 for gain calibration. We estimated the systematic flux uncertainty of  $\sim 10\%$  based on the amplitude and phase variations of the calibrators over time. Continuum images were created using the calibrated visibilities by averaging all the continuum channels, with natural weighting in *clean* (see the continuum images in Figure 1). The typical continuum beam size is  $1.''1 \times 0.''7$ , when all baselines are included. Self-calibration was not applied on these weak sources.

### 3. RESULTS

The continuum images for the 14 sources are shown in Figure 1. To measure continuum flux densities, we fit the visibility data using the CASA task *uvmodelfit*, following the description in [Barenfeld et al. \(2016\)](#). This model has three free parameters: the integrated flux density ( $F_\nu$ ), the phase center offsets in right ascension ( $\Delta\alpha$ ) and in declination ( $\Delta\delta$ ). Most sources are unresolved and are well-fit with a point-source model. The point-source models provide a good fit for low signal-to-noise detections and for sources with small aspect ratios. As in our Cycle 2 survey, elliptical models are also applied in *uvmodelfit* to all detected sources with a signal-to-noise larger than 5, with three additional parameters: the FWHM of the major axis, the aspect ratio, and the position angle. The elliptical Gaussian profiles provide a better fit and are adopted for only two sources, T16 and T24, for which lower flux uncertainties are ob-

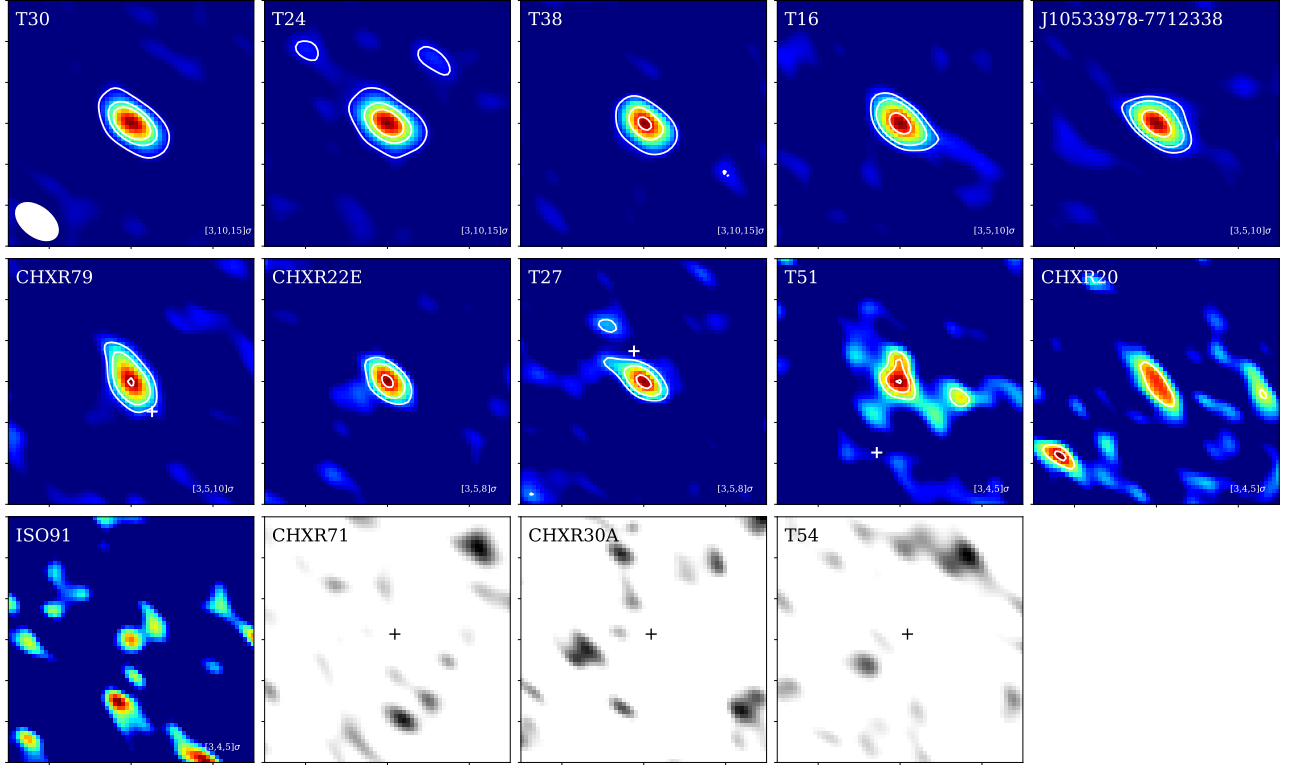


**Figure 1.** Continuum images at  $887\mu\text{m}$  for Cycle 3 sample, ordered by decreasing millimeter flux with colormap scaled by the peak flux of each source. Contour levels for each panel are labeled at the right corner. Images are  $6'' \times 6''$  with the typical beam size of  $1.''1 \times 0.''7$  shown in the top left panel. Close companions for CHXR79, T27, and T51 are marked with white crosses, with position angles adopted from [Daemgen et al. \(2013\)](#).

tained<sup>3</sup>. The uncertainties of the fitted parameters are scaled by the square root of the reduced  $\chi^2$  of the fit. The fitted fluxes and phase center offsets are consistent within the uncertainties for both the elliptical Gaussian and the point-source models.

Of the 14 observed sources in our Cycle 3 program, 11 are detected with a signal-to-noise ratio of  $>3$ . Table 2 summarizes the measured continuum flux densities and associated uncertainties ( $F_{mm}$ ), offsets from the phase center in right ascension and declination ( $\Delta\alpha$  and  $\Delta\delta$ ), and the source FWHMs for the two cases where an elliptical Gaussian model is adopted. Flux densities

<sup>3</sup> CHXR20 looks like an edge-on disk, but the elliptical Gaussian model from *uvmodelfit* returns a highly uncertain minor axis and *imfit* do not yield a deconvolved source size because of the low signal-to-noise.

that are brighter than three times the uncertainty and located near the expected source position are considered detections. The median values of  $\Delta\alpha = -0.''34$  and  $\Delta\delta = -0.''02$  from the detections are consistent with the values reported in [Pascucci et al. \(2016\)](#) in the full sample. These offsets from the 2MASS coordinates are roughly consistent with expectations based on proper motion ([Lopez Martí et al. 2013](#); [Murphy et al. 2013](#)).

Three sources remain undetected. For these sources (CHXR71, CHXR30A, and T54), the continuum emission is re-calculated by fitting a point-source model with fixed phase center offsets of  $\Delta\alpha = -0.''34$  and  $\Delta\delta = -0.''02$ . Table 2 lists the best-fit flux and uncertainty for these non-detections. These uncertainties do not include the 10% absolute flux calibration error.

**Table 2.** Source Properties and Measured Fluxes

2MASS	Name	Multiplicity (arcsec)	SpTy	$\log(M_*)$ ( $M_\odot$ )	$F_{mm}(P16)$ (mJy)	$F_{mm}$ (mJy)	$\Delta\alpha$ (arcsec)	$\Delta\delta$ (arcsec)	FWHM (arcsec)	$\log(M_{dust})$ ( $M_\oplus$ )
(1)	(2)	(3)	(4)	(5)	(6)	(7)	(8)	(9)	(10)	(11)
J10533978-7712338			M2	-0.41	4.60±0.79	3.74±0.16	-0.47±0.02	-0.04±0.01		0.24
J11023265-7729129	CHXR71	0.56	M3	-0.52	-0.21±0.82	-0.00±0.16	...	...		<-0.65
J11045701-7715569	T16		M3	-0.53	2.54±0.81	3.74±0.26	-0.34±0.02	-0.05±0.02	0.47×0.22	0.24
J11064510-7727023	CHXR20	28.46	K6	-0.03	0.53±0.82	0.93±0.16	-0.12±0.06	0.02±0.06		-0.36
J11070925-7718471	ISO91		M3	-0.52	0.06±0.82	0.65±0.17	0.34±0.09	-0.03±0.09		-0.51
J11071206-7632232	T24		M0	-0.23	4.23±0.81	6.57±0.25	-0.44±0.01	-0.04±0.01	0.33×0.11	0.49
J11071330-7743498	CHXR22E		M4	-0.63	0.42±0.81	2.23±0.16	-0.64±0.03	0.08±0.02		0.02
J11072825-7652118	T27	0.78	M3	-0.53	1.50±0.81	2.20±0.16	-0.15±0.03	-0.02±0.02		0.01
J11075809-7742413	T30		M3	-0.51	6.45±0.79	7.11±0.16	-0.37±0.01	0.00±0.01		0.52
J11080002-7717304	CHXR30A	0.46	K7	-0.18	-0.69±0.80	-0.07±0.15	...	...		<-0.67
J11085464-7702129	T38		M0.5	-0.18	3.90±0.79	4.03±0.16	-0.14±0.01	-0.11±0.01		0.28
J11091812-7630292	CHXR79	0.88	M0	-0.18	1.30±0.79	2.78±0.16	-0.26±0.02	0.09±0.02		0.12
J11122441-7637064	T51	1.97	K2	0.04	0.19±0.78	1.21±0.16	-0.39±0.05	-0.12±0.05		-0.24
J11124268-7722230	T54	0.24	K0	0.20	-0.02±0.79	-0.00±0.16	...	...		<-0.65

NOTE—References for stellar multiplicity are [Lafrenière et al. \(2008\)](#) and [Daemgen et al. \(2013\)](#). Spectral types are adopted from [Manara et al. \(2016, 2017\)](#) and stellar masses are adopted from [Pascucci et al. \(2016\)](#). Column 6 and 7 are 887 $\mu$ m fluxes in [Pascucci et al. \(2016\)](#) and this work. Phasecenter offsets in R.A. and Dec are listed in column 8 and 9. When an FWHM value is listed in column 10, the source is fitted with an elliptical Gaussian. Otherwise, a point-source model is applied. Dust masses in column 11 are calculated based on the same assumption as in [Pascucci et al. \(2016\)](#) and for a constant temperature of 20 K.

Six of the 11 detections here were undetected (at a  $3\sigma$  significance) in our Cycle 2 data. The signal-to-noise ratios of the detections improved by a factor of 5. Combining the observations presented in [Pascucci et al. \(2016\)](#) and in this paper, the detection rate for the *Hot* Sample is now 94% (51/54). The fluxes from Cycle 3 are generally higher than those observed in Cycle 2 (Figure 2), though consistent within 1-2 $\sigma$  uncertainties. The flux ratios of the sources detected in both observations range from 0.8–1.5, with an average value of 1.2. We note that the flux calibrator, Pallas, used in our Cycle 2 observations has been reported recently to be problematic due to model uncertainties (Daniel Harsono, priv. communication; see also more description in CASA Task *setjy*). In addition, the large phase variations in our shallow Cycle 2 observation affect the flux measurements for faint disks ([Carilli & Holdaway 1999](#)). The deeper Cy-

cle 3 flux measurement is therefore more reliable than that of Cycle 2.

Figure 3 (left panel) presents the millimeter flux densities and  $3\sigma$  upper limits as a function of stellar mass in the log-log plane. This figure is similar to Figure 6 in [Pascucci et al. \(2016\)](#), but updated with the 14 new fluxes in our Cycle 3 sample. The best-fit correlation between disk flux and stellar mass is  $\log(F_{mm}/\text{mJy}) = 1.89(\pm 0.24) \times \log(M_*/M_\odot) + 1.57(\pm 0.14)$ , assuming a linear scaling relation in the log-log plane and using a Bayesian linear regression method, following [Pascucci et al. \(2016\)](#)<sup>4</sup>. The fitted parameters

<sup>4</sup> [Pascucci et al. \(2016\)](#) used the [Kelly \(2007\)](#) IDL routine, while here we use the python equivalent *Linmix*, from <https://github.com/jmeyers314/linmix>. We refer the reader to Appendix A in [Pascucci et al. \(2016\)](#) for a description of how results from this method are consistent with results from a simpler linear regression.



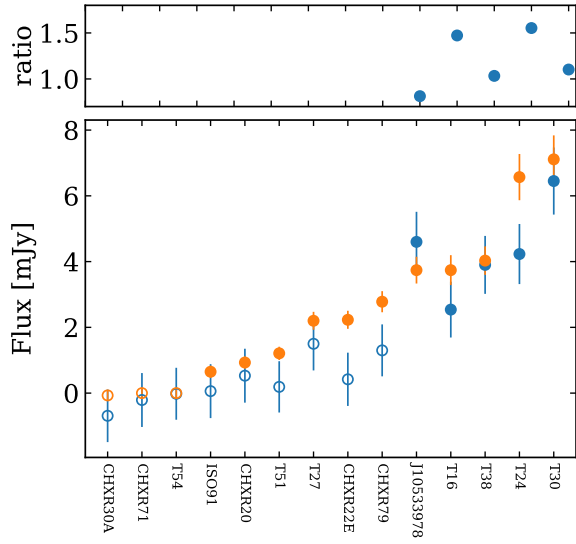


**Figure 2.** Bottom: Flux densities for Cycle 3 sources in order of increasing flux, with error bars including both the statistic uncertainty and the 10% absolute flux calibration uncertainty (added in quadrature). Blue symbols are results from Cycle 2, while orange for Cycle 3. Solid dots and open circle represent detection and non-detection; Top: Flux ratios for the 5 sources that are detected in both observations. The average ratio is 1.2.

are consistent with the best-fit values from Pascucci et al. (2016), with a slope of  $1.9 \pm 0.2$  and an intercept of  $1.6 \pm 0.1$  (see more details in Pascucci et al. (2016) for the fitting method).

These relationships are consistent because the scaling relation fits assume that the data points are scattered in a Gaussian distribution. With a higher detection rate, we confirm that this assumption is mostly correct, with some caveats. Figure 3 shows that the full range of disk mm flux is an order of magnitude at any given stellar mass. The offset between each data point and the fitted line shows a Gaussian fit with a mean value of 0.12 and  $1\sigma$  spread of 0.26 (see right panel of Figure 3). The fitted positive mean value (or offset) is due to the inclusion of upper limits with low fluxes. This fit

also reveals that four disks are outliers, with fluxes that are  $> 3\sigma$  fainter than the mean.

Since these four sources are anomalously faint, they may follow a different evolutionary path. A better fitting approach may be to exclude them from the scaling relation. When these four outliers, and a random sample of the same fraction (7%) of the upper limits in the cool sample, are excluded from the fit, we obtain a  $F_{mm} - M_{\star}$  scaling relation of  $\log(F_{mm}/\text{mJy}) = 2.07(\pm 0.21) \times \log(M_{\star}/M_{\odot}) + 1.81(\pm 0.13)$ . Therefore, excluding the outliers steepens the  $F_{mm} - M_{\star}$  correlation by  $1\sigma$  and increases the average disk mass by  $\sim 0.2$  dex in the *Hot* sample, though consistent within  $3\sigma$  of the uncertainty reported in Pascucci et al. (2016).

The correlation between disk mass (mm flux) and stellar mass depends on the model of stellar evolution used to estimate stellar mass. The stellar masses in this work are obtained from Pascucci et al. (2016), which were calculated by comparing stellar parameters (mostly from Manara et al. 2016 and Manara et al. 2017) to a combination of the Baraffe et al. (2015) models at low masses and the non-magnetic Feiden (2016) models<sup>5</sup> at higher masses. Use of the Feiden (2016) magnetic models would increase the stellar masses<sup>6</sup> by  $\sim 0.2$  dex (between  $0.1-0.9 M_{\odot}$ ), thereby shifting the correlation to higher masses (i.e., the intercept in the best-fit correlation between disk and stellar mass would decrease by  $\sim 0.4$ ). The updated distance has increased disk masses and stellar luminosities by 0.15 dex relative to Pascucci et al. (2016). Since most stars in our sample are fully convective and evolving along the near-vertical Hayashi track, the

<sup>5</sup> The non-magnetic models of Feiden (2016) were not available at the time of submission.

<sup>6</sup> Both models produce masses that correlate well with stellar masses, as measured from disk rotation (Guilloteau et al. 2014; Czekala et al. 2015; Simon et al. 2017; Yen et al. 2018) and young eclipsing binaries (see compilation by Stassun et al. 2014). Use of the Feiden magnetic models would also increase the age of Chamaeleon I by  $\sim 0.3$  dex.

mass is determined mostly by the spectral type (temperature) and is only minimally affected by the change in luminosity.

#### 4. FAINT DISKS

In the following section, we investigate the source properties of the faintest disks in our Cycle 3 sample. The four outliers identified in the previous section consist of two weak continuum detections (CHXR20 and T51) and two non-detections (CHXR30A and T54). Another two faint disks, ISO91 (a  $3.8\sigma$  detection) and CHXR71 (a non-detection), are not classified as anomalous outliers because of their lower stellar masses, but both have disk masses that are much lower than those of sources with similar stellar mass (see Figure 3) and are also included in this discussion.

Properties of these six sources are summarized in Table 3 and are discussed in detail below (see also the Appendix A for a more detailed description of individual sources), including their SEDs (Figure 4 and Figure 5), accretion properties, and stellar multiplicity. All six sources are classified as Class II objects based on their infrared spectral indices between  $2\ \mu\text{m}$  and  $24\ \mu\text{m}$  (Luhman et al. 2008).

##### 4.1. Non-detections at mm wavelengths

Figure 4 presents the SEDs for the three sources (CHXR71, CHXR30A, and T54) that are not detected in our ALMA observations. Their SEDs show little or no excess continuum emission at wavelengths  $\lesssim 8\ \mu\text{m}$ , indicating that their inner optically thick disks have mostly dissipated. The  $10\ \mu\text{m}$  silicate features in CHXR71 and T54 are weak or barely present, which suggests a deficit of small dust grains (Furlan et al. 2009) and/or a high degree of dust settling (Manoj et al. 2011). The dust mass upper limits are only  $\sim 0.2\ M_{\oplus}$ , comparable to the high mass end of dust masses in debris disks (Moór et al. 2017).

CHXR71, CHXR30A, and T54 have stellar companions located at projected separations of  $0.''56$ ,  $0.''46$ , and  $0.''24$  (Lafrenière et al. 2008; Daemen et al. 2013), respectively, corresponding to 106

AU, 87 AU, and 45 AU at the given distance of Chamaeleon I. In each system, the primary component dominates the UV and optical spectrum, from which the measured accretion rate is consistent with chromospheric activity (Manara et al. 2016, 2017).

##### 4.2. Weak detections at mm wavelength

The SEDs for the three weak detections (CHXR20, ISO91, and T51) are shown in Figure 5. T51 has a near-IR excess typical of many Class II disks, while CHXR20 shows no emission excess at wavelength  $\lesssim 6\ \mu\text{m}$ . The  $10\ \mu\text{m}$  silicate emission features are detected in both systems. The low  $13\text{--}31\ \mu\text{m}$  spectral index in T51 is explained by Furlan et al. (2009) and Manoj et al. (2011) as an outward truncation by the  $1.''9$  stellar companion (Lafrenière et al. 2008). CHXR20, however, is only accompanied by a very wide ( $28.''46$ ) companion (Kraus & Hillenbrand 2007), without any known close companion found from either high-resolution spectroscopy (Nguyen et al. 2012) or Adaptive Optics imaging (Lafrenière et al. 2008). Optical spectra obtained with VLT/X-Shooter demonstrate that both components of T51 are accreting at a rate expected for their spectral type, while CHXR 20 is weakly accreting (Manara et al. 2016, 2017; see further details in the Appendix).

For ISO91, even though mm continuum emission is only detected at  $4\sigma$ , the extreme extinction and the large-scale  $^{12}\text{CO}$  outflow (see  $^{12}\text{CO}$  channel maps in Appendix A) indicate that it may be at an earlier evolutionary stage, still surrounded by an envelope. ISO91 is therefore excluded in the further analysis.

## 5. DISCUSSION

The sample of faint disks discussed above covers a wide range of SED morphologies, accretion rates, and binarity. This diversity may refer to different evolutionary stages and/or different mechanisms in shaping the disk. In the following sections, we will first compare source properties of

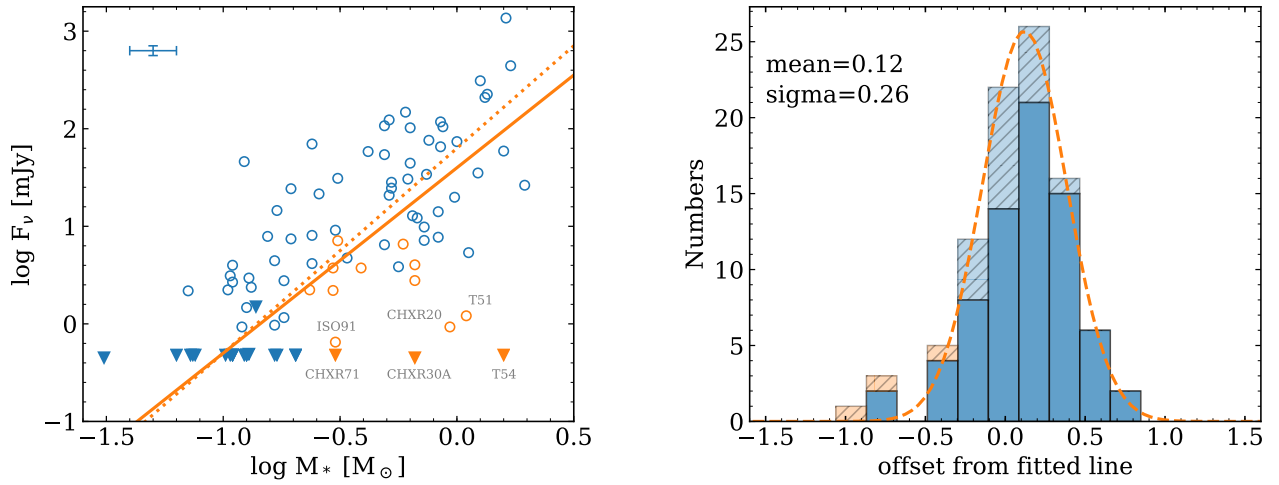


**Figure 3.** Left: Continuum flux densities as a function of stellar mass. The 14 sources re-observed in Cycle 3 are shown in orange, while the others are shown in blue with fluxes adopted from Cycle 2 observations (Pascucci et al. 2016). Open circles for detections and downward triangles for non-detections. The best fit relation (orange full line) using updated fluxes and upper limits are highly consistent with relation (almost overlapped thus not shown here) from Pascucci et al. (2016). Revised relation without considerable outliers (see text for how they are selected) is shown in dotted line. The median error bars for  $\log(M_*)$  and  $\log(F_{mm})$  are shown in the left upper corner and correspond to 0.1 dex and 0.05 dex; Right: Distribution of offsets from data points to the fitted line. Offsets in positive represent sources with higher continuum fluxes. Fitted parameters for the Gaussian distribution are labeled in text. The non-detections are shown in hatches to separate from the detections shown in full histogram, and the three Cycle 3 non-detections are shown in orange.

these faint disks to the entire Chamaeleon I sample, and then attempt to place each disk on its own evolutionary track based on source properties.

As a parallel effort to understand young stellar system evolution, Manara et al. (2016, 2017) measured mass accretion rates<sup>7</sup> for most sources in our ALMA Cycle 2 Chamaeleon I disk survey (Pascucci et al. 2016), based on UV continuum excess, or line luminosity when signal-to-noise ratio at short wavelength is poor. Accretion rates for the three non-detections (CHXR71, CHXR30A, and T54) in the *Hot* sample are all below or close to the expected emission from chromosphere (see

<sup>7</sup> The mass accretion rates used here are scaled to the new Gaia DR2 distance  $d$  of 190 pc by multiplying by  $\left(\frac{190 \text{ pc}}{160 \text{ pc}}\right)^3 = 1.67$ , since the accretion rate is proportional to the accretion luminosity ( $\propto d^2$ ) and stellar radius ( $\propto d^1$ ).

Figure 6)<sup>8</sup>, indicating that any on-going accretion is weak. The uncertainties in accretion rate are typically  $\sim 0.3$  dex and are more uncertain near the chromospheric boundary<sup>9</sup>. The other two faint sources, CHXR20 and T51 (marked with a downward arrow in Figure 6), have contradictory accretion rate measurements in the literature but are established by X-Shooter spectra to be accreting (e.g. Manara et al. 2016, 2017). Meanwhile, the vast majority of continuum detections have accretion

<sup>8</sup> 2MASS J10533978-7712338 is located far below the plot boundary and is likely an edge-on disk (Luhman 2007), thus its stellar properties and measured accretion rate are highly uncertain and not trustworthy, and is excluded from the plot.

<sup>9</sup> Herczeg & Hillenbrand (2008), Alcalá et al. (2014), and Manara et al. (2016) provide detailed discussions on the uncertainties in these measurements, while Costigan et al. (2014) and Venuti et al. (2015) quantify variability in accretion rate measurements.



**Table 3.** Source Properties For Faint Disks

Name	Multiplicity (arcsec)	Accretion	IR excess	mm detection	possible explanations
(1)	(2)	(3)	(4)	(5)	(6)
CHXR71	0.56	No	weak	No	tidal truncation / internal photoevaporation
CHXR30A	0.46	No	weak	No	tidal truncation / internal photoevaporation
T54	0.24	No	weak	No	tidal truncation / internal photoevaporation
CHXR20	28.46	Yes?	weak	Yes	grain growth
T51	1.97	Yes?	normal	Yes	tidal truncation

NOTE—Accretion measurements in literature for CHXR20 and T51 show contradictory results, so marked with “?”. See more details in Appendix A.

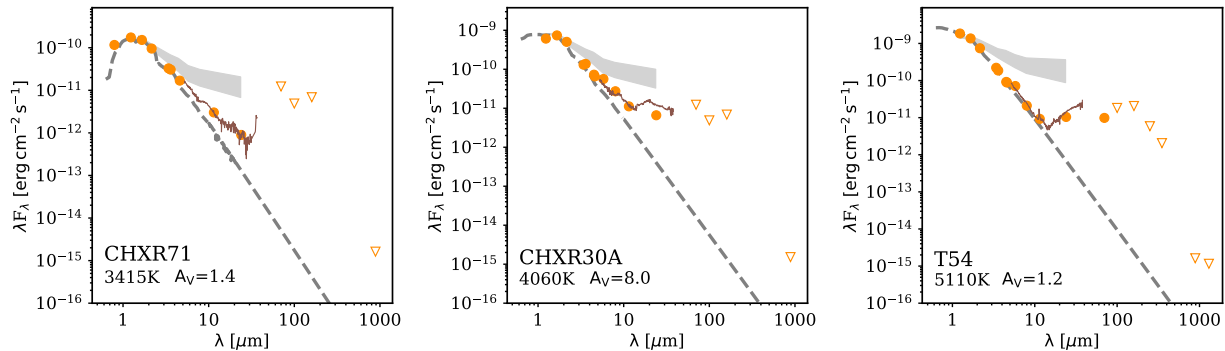


**Figure 4.** SEDs for the three sources in which  $887 \mu\text{m}$  are not detected in our Cycle 3 observation. The  $T_{\text{eff}}$  and  $A_V$  are adopted from Manara et al. (2017). We show here the extinction-corrected optical and infrared photometry (Epchtein et al. 1999; Skrutskie et al. 2006; Luhman 2007), *Spitzer* IRS spectra and ALMA upper limits. *Herschel* upper limits are adopted from the average measurements or upper limits in Chamaeleon I samples (Olofsson et al. 2013), except data for T54, which is adopted from Matrà et al. (2012). We also include the 1.3 mm upper limits for T54 from Hardy et al. (2015). The light gray filled region shows the upper and lower quartiles of the median SEDs of L1641 ( $\sim 1.5$  Myr) CTTSs with similar spectral type to each source (Fang et al. 2013), normalized at the *H*-band flux of each source. The dashed gray lines are the NextGen stellar model (Hauschildt et al. 1999; Allard et al. 2000) at specified  $T_{\text{eff}}$  which are normalized to *J*-band flux.

rates much higher than the typical chromospheric emission. CHXR22E, however, stands out as an exception with detected millimeter emission and no detected accretion. CHXR22E is classified as a transitional disk candidate in Kim et al. (2009) without a near-infrared excess (also see Figure 10). CHXR22E also has no reported close stellar companion (Lafrenière et al. 2008). Since accretion is variable and our accretion rates are from single

epochs, the rates do not necessarily correspond to the time-averaged accretion onto these objects.

The three non-detections are close binaries with projected separations of 40–100 AU. The weakly detected source, T51, also has a stellar companion separated by at least  $\sim 360$  AU. Based on unresolved disk diagnostics, disk lifetimes in close binaries (with separation  $\lesssim 40$  AU) are shorter than lifetimes of disks around single stars (Bouwman

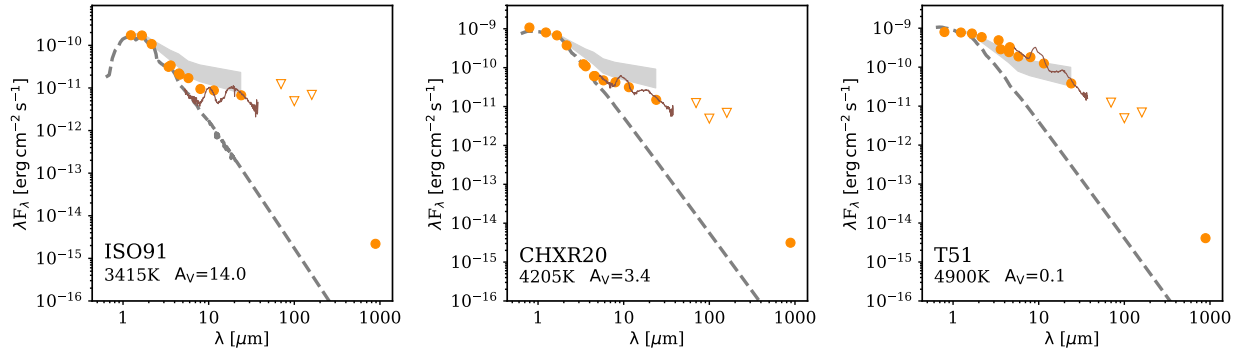


**Figure 5.** Same as Figure 4, but for the 3 sources in which 887  $\mu\text{m}$  emission are only weakly detected.

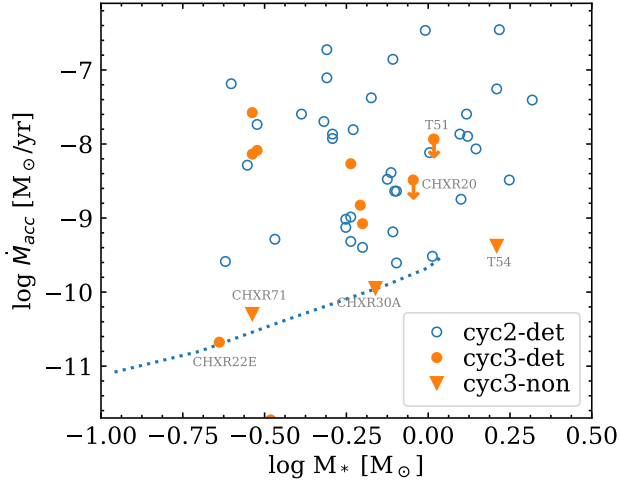


**Figure 6.** Mass accretion rate for the Cycle 2 and Cycle 3 detections are marked with blue open circles and orange dots, respectively. The typical upper limit on accretion rate versus stellar mass (dotted line) is calculated by Manara et al. (2013) based on the intensity of line emission in non-accreting young stellar objects. All of the three millimeter non-detections are not accreting at detectable level.

et al. 2006; Cieza et al. 2009; Kraus et al. 2012; Daemgen et al. 2016). From component-resolved millimeter observations in a large sample of disks in Taurus, flux densities decrease significantly as a function of decreasing pair separation (Harris et al. 2012). More specifically, Harris et al. (2012) found substantially lower flux densities at projected separations of 30 AU and 300 AU. As seen from Fig-

ure 7, this trend is not prominent in Chamaeleon I, though binary systems with small separations ( $\lesssim 30$  AU, if excluding the spectroscopic binary – WW Cha) have lower average millimeter flux. The spectroscopic binary, WW Cha (marked in Figure 7), is the brightest continuum source in our sample (Pascucci et al. 2016), consistent with the trend found in Harris et al. (2012) that circumbinary disks around spectroscopic binaries tend to have higher fluxes. We note that systems with projected separations  $\lesssim 100$  AU should remain unresolved at our spatial resolution. If both individual disks exist, millimeter fluxes for small separation systems should be lower than the value reported here.

In the following subsections, we discuss physical mechanisms that could explain the evolutionary stage of these mm-faint sources. We start with possible explanations for individual disk evolutions, since our binaries are largely unresolved and most likely to retain their own circumstellar disks at a separation of  $\sim 100$  AU. We then discuss disk evolution in binary systems and the possibility of a disk around the fainter secondary star.

### 5.1. Individual disk evolution

As disk mass and accretion rate decrease over time, photoevaporation becomes the leading role in draining the inner disk and eventually creates inner cavities (Alexander et al. 2014). Once the inside-out dissipation begins, accretion ceases quickly as

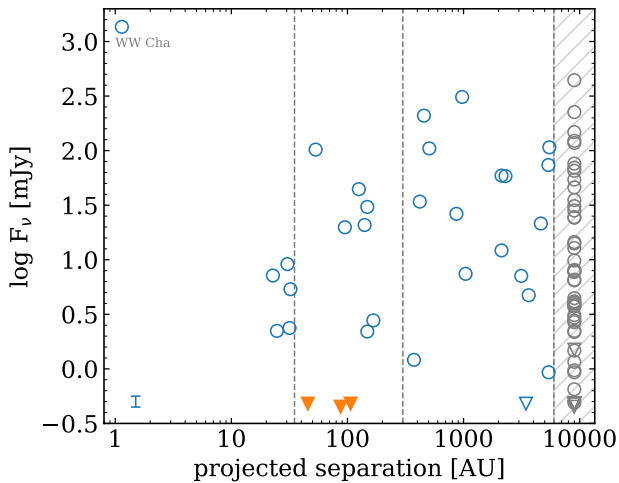


**Figure 7.** millimeter flux densities as a function of projected binary separation. Single stars are shown in the right hatched region for reference. The three *Hot* sample non-detections are highlighted in orange downward triangles. The two vertical gray dashed lines represent 30 AU and 300 AU, as proposed in Harris et al. (2012) to group the Taurus sample. The median error bar for  $\log(F_{mm})$  is 0.05 dex and shown in the left lower corner.

material from the outer disk can not pass through the photoevaporation front. Observationally, most WTTSs show little or no near-IR excess at wavelength  $\lesssim 6 \mu\text{m}$  (Padgett et al. 2006; McCabe et al. 2006; Manoj et al. 2011). The three disks in this paper that are not detected at  $887 \mu\text{m}$  are also not accreting at detectable level and have SEDs that indicate some clearing of the inner disk, both consistent with internal photoevaporation. Kim et al. (2009) modeled an inner dust disk cavity of 37 AU for T54, which is broadly consistent with the predicted size of the inner disk hole from photoevaporation models driving by EUV+X-ray radiation at its given upper limit of accretion rate (see more details in Figure 6 of Ercolano & Pascucci 2017). Comparisons with photoevaporation models for CHXR71 and CHXR30A are limited by the lack of previous studies.

Starting from a primordial flared disk, larger particles formed by collisional coagulation feel

less thermal pressure support and settle towards the disk mid-plane (Weidenschilling 1977). Fast grain growth is expected in the denser regions through which small particles are gradually depleted, thereby leading to a strong decrease of flux densities from near to mid-infrared wavelengths (Dullemond & Dominik 2005; D’Alessio et al. 2006). This overall decrease in the level of excess emission across the disk SED resembles the so-called “evolved” disk (Lada et al. 2006; Hernández et al. 2007; Currie et al. 2009; Luhman et al. 2010). A wide range of accretion rate and disk mass are reported for such disks (Cieza et al. 2012). Instead of a sharp rise in the mid-infrared wavelength region ( $>10 \mu\text{m}$ ), as is typical for transition disks, CHXR20 and the three non-detection sources show weaker mid-infrared excesses. Fast grain growth is capable of explaining the observed SED morphologies in these four disks, indicating disk evolution by grain growth instead of direct disk dissipation.

### 5.2. Disk evolution in binary systems

A stellar companion orbiting the primary star, separated by a typical disk radius, can dramatically alter the disk structure and its evolution. Strong tidal interactions truncate the disk radii and reduce disk masses (Jensen et al. 1994, 1996; Harris et al. 2012; Akeson & Jensen 2014). Theoretical models predict the fate for each of the three disks in a binary system (i.e., circumprimary, circumsecondary, and circumbinary) in a range of stellar and disk configurations (mass ratio  $q$ , semi-major axis  $a$ , orbital eccentricity  $e$  and disk viscosity  $\alpha$ ) (Papaloizou & Pringle 1977; Artymowicz & Lubow 1994; Miranda & Lai 2015; Lubow et al. 2015). The classical calculation for a co-planar binary in Artymowicz & Lubow (1994) predicts an outer truncation for circumstellar disks at  $\sim 0.3a$  and an inner truncation for circumbinary disks of  $\sim 2-3a$ , though disk truncation for misaligned systems are not fully explored (e.g., Miranda & Lai 2015).

According to disk truncation models, the  $\sim 2''$  companion in T51 would have truncated the outer circumstellar disk at a radius of  $\sim 100-150$  AU.

Given the large beam size ( $\sim 100$  AU in radius) in our observations, the disk size is not well constrained.

Stellar companions for the three non-detections, T54, CHXR30A, and CHXR71, are separated in projected distance by 45, 87, and 106 AU, respectively. Individual disks must have undergone tidal stirring in these systems. Given the binary separations, circumbinary disks are more plausible to be present for T54 than for CHXR71 and CHXR30A. [Espaillat et al. \(2017\)](#) reproduced the IR SED of T54 with a model consisting of a circumprimary disk ( $\sim 10$  AU) and a circumbinary disk (60–100 AU). Tidal truncation in the outer disk and photoevaporation in the inner edge could cooperate together to explain non-detections in both millimeter emission and accretion for the three sources.

Close companions ( $\lesssim 40$ –100 AU) can shorten disk lifetimes ([Cieza et al. 2009](#); [Kraus et al. 2012](#)) and reduce disk masses ([Harris et al. 2012](#); [Cox et al. 2017](#)), which should have direct consequences on planets formed within. Despite such a hostile environment, many planets have been detected in circumstellar orbits of binary systems in a wide range of separations (e.g., [Eggenberger et al. 2007](#)), in addition to extreme cases like multiple rocky planets in binaries (e.g., Kepler-444, [Dupuy et al. 2016](#)). Though the overall binary fraction of *Kepler* exoplanet host stars is estimated to be comparable to the general field population ( $\sim 40\%$ ) ([Horch et al. 2014](#)), planet formation is strongly suppressed around binary hosts with separation from  $\sim 20$  AU up to 100 AU ([Eggenberger et al. 2007](#); [Bonavita & Desidera 2007](#); [Wang et al. 2014](#); [Kraus et al. 2016](#)). This difference is expected to be a direct consequence of the faster disk dispersal in binary systems, though grain growth in binary systems with tens of AU separations is indistinguishable from single stars ([Pascucci et al. 2008](#)). The above statistics only applies to circumstellar planets, leaving circumbinary planets untouched.

### 5.3. Disks around the secondary star

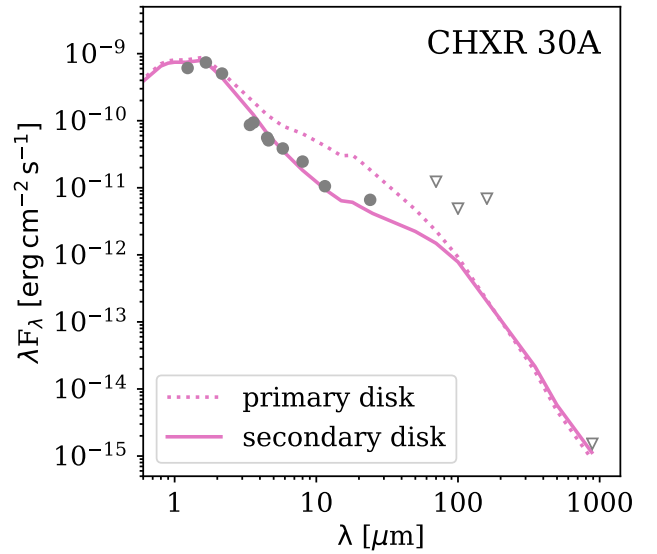


**Figure 8.** Modeled SED for CHXR30A. Solid line represents scenario of disk around the faint secondary, while dotted line for disk around the primary.

In unequal-mass binary systems, the disk could survive longer around the secondary star than around the primary star, as has been found for several systems with mid-IR imaging ([McCabe et al. 2006](#)). Disks around cool stars and sun-like stars are quite different in physical and chemical structures (e.g., [Pascucci et al. 2009](#); [Szűcs et al. 2010](#)), though similar dust properties are able to explain the observed median IR SEDs across a range of stellar mass ([Mulders & Dominik 2012](#)). Very low mass stars and brown dwarfs have flatter disks and overall less excess at IR bands (e.g., [Apai et al. 2005](#); [Liu et al. 2015](#)), with SEDs similar to Figure 4. If the disk is around the fainter secondary star, the weaker radiation field should result in less emission at all IR bands, compared to the case of disk around the primary star. In unresolved observations, the photospheric emission from the primary star would dominate at all short wavelengths, until somewhere in the mid-IR where the dust is brighter. Accretion from the secondary star is therefore hard to be detectable in the optical spectra.

If the disk is around the secondary star, the disk may be weak or undetected in the sub-mm because (a) disks around lower-mass objects are expected to be less massive (Figure 3), and (b) the disk will also be colder than assessed because of the weaker radiation field of the lower-mass star. To test the possibility of a disk around the secondary star in a binary system, we use the radiative transfer code RADMC-3D (Dullemond et al. 2012) to model the SED of the binary system CHXR30A. Stellar properties for the primary star are adopted from Manara et al. (2017). The  $K_s$ -band contrast of 0.85 from (Lafrenière et al. 2008) leads to an estimated stellar mass of  $0.28 M_{\odot}$ <sup>10</sup>. Based on the projected separation, the two stellar components are placed at 80 AU apart. The secondary disk is therefore truncated at  $\sim 30$  AU<sup>11</sup>, following predictions from the evolution of disks in binaries (Artymowicz & Lubow 1994). The ratio of disk mass<sup>12</sup> to stellar mass is adjusted to satisfy the millimeter flux upper limit.

The modeled SED reproduces well the observed SED structure, as shown in Figure 8. In this scenario, the dust continuum emission at  $887 \mu\text{m}$  is still fainter, by a factor of few than expected from the stellar mass-disk mass correlations, due to a truncated outer disk. If we keep most of the disk parameters fixed, but place the disk around the primary star and reduce the disk mass to satisfy the mm flux upper limit, the emission at IR wavelength would be brighter by an order of magnitude.

While identifying the best-fit model for these systems is beyond the scope of this paper, this experiment verifies the possibility that a circumsecondary disk may explain the observed stellar SEDs

<sup>10</sup> The mass and luminosity are actually upper limits, since these calculations assume that the  $K$ -band emission from the secondary star does not include any disk emission.

<sup>11</sup> The truncation radius could be lower limit, if the real binary separation is wider than the projected separation.

<sup>12</sup> In the disk model, we include two populations of amorphous dust grains with 25% carbon and 75% silicate, resulting in a dust opacity a few times higher than what used in disk dust mass calculation (Pascucci et al. 2016).

of our mm-faint binary systems. Binary systems, where the disk is around the secondary star, may confuse models of disk evolution because these systems are rare enough to not dominate the population statistics, but are common enough to be identified as outliers that could link different evolutionary states. For example, the star CZ Tau AB is a  $0.3 M_3 + \sim M_6$  binary system with an SED with no near-IR excess, a sharp rise from  $5\text{--}20 \mu\text{m}$ , then a rapid falloff at longer wavelengths (Furlan et al. 2006) and a non-detection in the sub-mm (Andrews et al. 2013). The optical spectrum shows no accretion from the primary (Herczeg & Hillenbrand 2014), but the secondary is faint enough to not contribute significantly to optical spectra. The  $K$ - and  $L$ -band imaging of McCabe et al. (2006) shows that the disk is likely around the secondary, a simple scenario that (along with disk truncation in Furlan et al. 2006) explains all of the existing observations without requiring any speculation about the CZ Tau disk being in a unique evolutionary stage of disk dispersal.

Rosotti & Clarke (2018) predict that disks around the secondary in wide binary systems ( $\gtrsim 30$  AU) could be longer lived than disks around the primary, possibly due to the lower X-ray photoevaporation rate around lower mass stars. ALMA observations have also discovered binary systems with mm-brighter circumsecondary disk than circumprimary disk (Akeson & Jensen 2014). Given the binary separation, the scenario of disk around the fainter secondary is more likely to explain the observations for CHXR30A and CHXR71 than for the closer T54 system.

Current ALMA disk surveys of disk mass in near-complete or unbiased samples in nearby regions have spatial resolutions of  $\sim 60\text{--}100$  AU, leaving disks in multiple systems unresolved. High-resolution ALMA observations towards large binary samples in different star-forming regions are needed to draw a comprehensive picture of disk demographics in multiple star/disk systems. Any correlation of circumstellar or circumbinary disk to



stellar mass ratio, binary separation or even the individual disk mass/size, if they exist, are worthy of an in-depth investigation for a better understanding of planetary architectures.

## 6. SUMMARY

In this paper, we presented 887  $\mu\text{m}$  ALMA Cycle 3 observations for 14 Class II disks in the nearby  $\sim 2$  Myr-old Chamaeleon I star-forming region. These targets were selected based on spectral type (earlier than or equal to M3), the presence of a disk in mid-IR observations, and having a faint detection or non-detection in our ALMA Cycle 2 program (Pascucci et al. 2016). We have identified mm-faint outliers in the high-sensitivity data and explored source properties from IR SED, accretion and stellar multiplicity. Our main findings are as follows:

1. By improving the sensitivity by a factor of 5, we identify six more sources with dust continuum emission and increase the detection rate to 94% (51/54) in the Chamaeleon I *Hot* sample.
2. We find that the stellar-disk mass relation reported in Pascucci et al. (2016) is robust to the inclusion of updated millimeter fluxes and upper limits for the faint sources. We identify mm-faint outliers which are located far from the main sample in the  $F_{mm} - M_*$  plot. Excluding these outliers yields a  $F_{mm} - M_*$  relation that is  $1\sigma$  steeper and an average disk mass that is  $\sim 0.2$  dex higher.
3. The three millimeter non-detections (CHXR71, CHXR30A, and T54) show little or no NIR excess and weaker MIR excess than typical Class II objects. These stars have mostly stopped accreting and are all accompanied by a stellar companion at projected separation  $\lesssim 100$  AU. We suggest that the combined effects of tidal interactions and internal photoevaporation hastens the overall disk evolution in these systems. The other

three weak detections (ISO91, CHXR20, and T51) have a wide variety of source properties. CHXR20 might have undergone fast grain growth which depletes small particles especially  $\mu\text{m}$ -sized particles in the near to mid-IR wavelength and even grow to cm-size. The faint millimeter flux for T51 could also be explained by a disk around the  $\sim 2''$  companion.

4. We also propose a scenario in which only a disk around the secondary star is left in a binary system to explain our observations. For CHXR30A, the model SED that includes only a circumsecondary disk matches the observations quite well. Such configurations may be common for binaries with separations  $\sim 30\text{--}100$  AU.

Binarity information is critical when evaluating rare objects, such as weak-lined T Tauri stars with disks (e.g., Wahhaj et al. 2010), both because of the exciting role that binarity may play in disk evolution (e.g., Kraus et al. 2012), but also because disk evolution may be confused by a circumsecondary disk. Stellar multiplicity contributes significantly in explaining the wide range of disk mm fluxes at any given stellar mass bin in a single cluster, but it is definitely not enough for the whole picture. Given the complexity in star+disk system, a better understanding of disk fundamental properties (e.g., disk size, inclination, dust grain properties) is needed as the next first step in characterizing disk evolution.

We would like to thank the anonymous referee for providing constructive comments that improved the quality of this manuscript. F.L. thanks Min Fang and Yao Liu for their help in RADMC modeling. F.L. and G.J.H are supported by general grants 11473005 and 11773002 awarded by the National Science Foundation of China. I.P. and N.H. acknowledges support from an NSF Astronomy & Astrophysics Research Grant ( ID: 1515392).

This paper makes use of the following ALMA data: ADS/JAO.ALMA#2015.1.00333.S. ALMA is a partnership of ESO (representing its member states), NSF (USA) and NINS (Japan), together

with NRC (Canada) and NSC and ASIAA (Taiwan), in cooperation with the Republic of Chile. The Joint ALMA Observatory is operated by ESO, AUI/NRAO and NAOJ.

## REFERENCES

- Akeson, R. L., & Jensen, E. L. N. 2014, *ApJ*, 784, 62
- Alcalá, J. M., Natta, A., Manara, C. F., et al. 2014, *A&A*, 561, A2
- Alexander, R., Pascucci, I., Andrews, S., Armitage, P., & Cieza, L. 2014, *Protostars and Planets VI*, 475
- Allard, F., Hauschildt, P. H., & Schweitzer, A. 2000, *ApJ*, 539, 366
- Andrews, S. M., Rosenfeld, K. A., Kraus, A. L., & Wilner, D. J. 2013, *ApJ*, 771, 129
- Ansdell, M., Williams, J. P., Manara, C. F., et al. 2017, *AJ*, 153, 240
- Ansdell, M., Williams, J. P., van der Marel, N., et al. 2016, *ApJ*, 828, 46
- Apai, D., Pascucci, I., Bouwman, J., et al. 2005, *Science*, 310, 834
- Artymowicz, P., & Lubow, S. H. 1994, *ApJ*, 421, 651
- Baraffe, I., Homeier, D., Allard, F., & Chabrier, G. 2015, *A&A*, 577, A42
- Barenfeld, S. A., Carpenter, J. M., Ricci, L., & Isella, A. 2016, *ApJ*, 827, 142
- Bonavita, M., & Desidera, S. 2007, *A&A*, 468, 721
- Bouwman, J., Lawson, W. A., Dominik, C., et al. 2006, *ApJL*, 653, L57
- Calvet, N., D’Alessio, P., Watson, D. M., et al. 2005, *ApJL*, 630, L185
- Carilli, C. L., & Holdaway, M. A. 1999, *Radio Science*, 34, 817
- Cieza, L. A., Schreiber, M. R., Romero, G. A., et al. 2012, *ApJ*, 750, 157
- Cieza, L. A., Padgett, D. L., Allen, L. E., et al. 2009, *ApJL*, 696, L84
- Clarke, C. J., Gendrin, A., & Sotomayor, M. 2001, *MNRAS*, 328, 485
- Correia, S., Zinnecker, H., Ratzka, T., & Sterzik, M. F. 2006, *A&A*, 459, 909
- Costigan, G., Vink, J. S., Scholz, A., Ray, T., & Testi, L. 2014, *MNRAS*, 440, 3444
- Covino, E., Alcalá, J. M., Allain, S., et al. 1997, *A&A*, 328, 187
- Cox, E. G., Harris, R. J., Looney, L. W., et al. 2017, *ApJ*, 851, 83
- Currie, T., Lada, C. J., Plavchan, P., et al. 2009, *ApJ*, 698, 1
- Czekala, I., Andrews, S. M., Jensen, E. L. N., et al. 2015, *ApJ*, 806, 154
- Daemgen, S., Elliot Meyer, R., Jayawardhana, R., & Petr-Gotzens, M. G. 2016, *A&A*, 586, A12
- Daemgen, S., Petr-Gotzens, M. G., Correia, S., et al. 2013, *A&A*, 554, A43
- D’Alessio, P., Calvet, N., Hartmann, L., Franco-Hernández, R., & Servín, H. 2006, *ApJ*, 638, 314
- Duchêne, G., & Kraus, A. 2013, *ARA&A*, 51, 269
- Dullemond, C. P., & Dominik, C. 2005, *A&A*, 434, 971
- Dullemond, C. P., Juhasz, A., Pohl, A., et al. 2012, *RADMC-3D: A multi-purpose radiative transfer tool*, *Astrophysics Source Code Library*, , , ascl:1202.015
- Dunham, M. M., Allen, L. E., Evans, Neal J., I., et al. 2015, *The Astrophysical Journal Supplement Series*, 220, doi:10.1088/0067-0049/220/1/11
- Dupuy, T. J., Kratter, K. M., Kraus, A. L., et al. 2016, *ApJ*, 817, 80
- Durisen, R. H., Boss, A. P., Mayer, L., et al. 2007, *Protostars and Planets V*, 607
- Eggenberger, A., Udry, S., Chauvin, G., et al. 2007, *A&A*, 474, 273
- Epchtein, N., Deul, E., Derriere, S., et al. 1999, *A&A*, 349, 236
- Ercolano, B., & Pascucci, I. 2017, *Royal Society Open Science*, 4, 170114
- Espaillet, C., Calvet, N., D’Alessio, P., et al. 2007, *ApJL*, 664, L111
- Espaillet, C. C., Ribas, Á., McClure, M. K., et al. 2017, *ApJ*, 844, 60
- Fang, M., Kim, J. S., van Boekel, R., et al. 2013, *ApJS*, 207, 5
- Fedele, D., van den Ancker, M. E., Henning, T., Jayawardhana, R., & Oliveira, J. M. 2010, *A&A*, 510, A72
- Feiden, G. A. 2016, *A&A*, 593, A99

- Frasca, A., Biazzo, K., Lanzafame, A. C., et al. 2015, *A&A*, 575, A4
- Furlan, E., Hartmann, L., Calvet, N., et al. 2006, *ApJS*, 165, 568
- Furlan, E., Watson, D. M., McClure, M. K., et al. 2009, *ApJ*, 703, 1964
- Gaia Collaboration, Brown, A. G. A., Vallenari, A., et al. 2018, *ArXiv e-prints*, arXiv:1804.09365
- Guilloteau, S., Simon, M., Piétu, V., et al. 2014, *A&A*, 567, A117
- Haisch, Jr., K. E., Lada, E. A., & Lada, C. J. 2001, *ApJL*, 553, L153
- Hardy, A., Caceres, C., Schreiber, M. R., et al. 2015, *A&A*, 583, A66
- Harris, R. J., Andrews, S. M., Wilner, D. J., & Kraus, A. L. 2012, *ApJ*, 751, 115
- Hartmann, L., Calvet, N., Gullbring, E., & D'Alessio, P. 1998, *ApJ*, 495, 385
- Hauschildt, P. H., Allard, F., Ferguson, J., Baron, E., & Alexander, D. R. 1999, *ApJ*, 525, 871
- Herczeg, G. J., & Hillenbrand, L. A. 2008, *ApJ*, 681, 594
- . 2014, *ApJ*, 786, 97
- Hernández, J., Calvet, N., Briceño, C., et al. 2007, *ApJ*, 671, 1784
- Horch, E. P., Howell, S. B., Everett, M. E., & Ciardi, D. R. 2014, *ApJ*, 795, 60
- Jensen, E. L. N., Mathieu, R. D., & Fuller, G. A. 1994, *ApJL*, 429, L29
- . 1996, *ApJ*, 458, 312
- Kelly, B. C. 2007, *ApJ*, 665, 1489
- Kim, K. H., Watson, D. M., Manoj, P., et al. 2009, *ApJ*, 700, 1017
- Kraus, A. L., & Hillenbrand, L. A. 2007, *ApJ*, 662, 413
- Kraus, A. L., Ireland, M. J., Hillenbrand, L. A., & Martinache, F. 2012, *ApJ*, 745, 19
- Kraus, A. L., Ireland, M. J., Huber, D., Mann, A. W., & Dupuy, T. J. 2016, *AJ*, 152, 8
- Lada, C. J., Muench, A. A., Luhman, K. L., et al. 2006, *AJ*, 131, 1574
- Lafrenière, D., Jayawardhana, R., Brandeker, A., Ahmic, M., & van Kerkwijk, M. H. 2008, *ApJ*, 683, 844
- Lissauer, J. J., & Stevenson, D. J. 2007, *Protostars and Planets V*, 591
- Liu, Y., Joergens, V., Bayo, A., Nielbock, M., & Wang, H. 2015, *A&A*, 582, A22
- Lodato, G., Scardoni, C. E., Manara, C. F., & Testi, L. 2017, *MNRAS*, 472, 4700
- Long, F., Herczeg, G. J., Pascucci, I., et al. 2017, *ApJ*, 844, 99
- Lopez Martí, B., Jimenez Esteban, F., Bayo, A., et al. 2013, *A&A*, 551, A46
- Lubow, S. H., Martin, R. G., & Nixon, C. 2015, *ApJ*, 800, 96
- Luhman, K. L. 2004, *ApJ*, 602, 816
- . 2007, *ApJS*, 173, 104
- Luhman, K. L., Allen, P. R., Espaillat, C., Hartmann, L., & Calvet, N. 2010, *ApJS*, 186, 111
- Luhman, K. L., Allen, L. E., Allen, P. R., et al. 2008, *ApJ*, 675, 1375
- Manara, C. F., Fedele, D., Herczeg, G. J., & Teixeira, P. S. 2016, *A&A*, 585, A136
- Manara, C. F., Testi, L., Rigliaco, E., et al. 2013, *A&A*, 551, A107
- Manara, C. F., Testi, L., Herczeg, G. J., et al. 2017, *A&A*, 604, A127
- Manoj, P., Kim, K. H., Furlan, E., et al. 2011, *ApJS*, 193, 11
- Matrà, L., Merín, B., Alves de Oliveira, C., et al. 2012, *A&A*, 548, A111
- McCabe, C., Ghez, A. M., Prato, L., et al. 2006, *ApJ*, 636, 932
- Merín, B., Brown, J. M., Oliveira, I., et al. 2010, *ApJ*, 718, 1200
- Miranda, R., & Lai, D. 2015, *MNRAS*, 452, 2396
- Moór, A., Curé, M., Kóspál, Á., et al. 2017, *ApJ*, 849, 123
- Mulders, G. D., & Dominik, C. 2012, *A&A*, 539, A9
- Mulders, G. D., Pascucci, I., Manara, C. F., et al. 2017, *ApJ*, 847, 31
- Murphy, S. J., Lawson, W. A., & Bessell, M. S. 2013, *MNRAS*, 435, 1325
- Nguyen, D. C., Brandeker, A., van Kerkwijk, M. H., & Jayawardhana, R. 2012, *ApJ*, 745, 119
- Olofsson, J., Szűcs, L., Henning, T., et al. 2013, *A&A*, 560, A100
- Owen, J. E., Clarke, C. J., & Ercolano, B. 2012, *MNRAS*, 422, 1880
- Padgett, D. L., Cieza, L., Stapelfeldt, K. R., et al. 2006, *ApJ*, 645, 1283
- Papaloizou, J., & Pringle, J. E. 1977, *MNRAS*, 181, 441
- Pascucci, I., Apai, D., Hardegree-Ullman, E. E., et al. 2008, *ApJ*, 673, 477
- Pascucci, I., Apai, D., Luhman, K., et al. 2009, *ApJ*, 696, 143
- Pascucci, I., Testi, L., Herczeg, G. J., et al. 2016, *ApJ*, 831, 125

- Pinilla, P., van der Marel, N., Pérez, L. M., et al. 2015, *A&A*, 584, A16
- Reipurth, B., & Zinnecker, H. 1993, *A&A*, 278, 81
- Ribas, Á., Espaillat, C. C., Macías, E., et al. 2017, *ApJ*, 849, 63
- Rosotti, G. P., & Clarke, C. J. 2018, *MNRAS*, 473, 5630
- Sacco, G. G., Spina, L., Randich, S., et al. 2017, *A&A*, 601, A97
- Simon, M., Guilloteau, S., Di Folco, E., et al. 2017, *ApJ*, 844, 158
- Skrutskie, M. F., Cutri, R. M., Stiening, R., et al. 2006, *AJ*, 131, 1163
- Stassun, K. G., Feiden, G. A., & Torres, G. 2014, *NewAR*, 60, 1
- Szűcs, L., Apai, D., Pascucci, I., & Dullemond, C. P. 2010, *ApJ*, 720, 1668
- Venuti, L., Bouvier, J., Irwin, J., et al. 2015, *A&A*, 581, A66
- Voirin, J., Manara, C. F., & Prusti, T. 2017, *ArXiv e-prints*, arXiv:1710.04528
- Wahhaj, Z., Cieza, L., Koerner, D. W., et al. 2010, *ApJ*, 724, 835
- Wang, J., Xie, J.-W., Barclay, T., & Fischer, D. A. 2014, *ApJ*, 783, 4
- Weidenschilling, S. J. 1977, *MNRAS*, 180, 57
- Yen, H.-W., Koch, P. M., Manara, C. F., Miotello, A., & Testi, L. 2018, *ArXiv e-prints*, arXiv:1804.06272
- Zhu, Z., Nelson, R. P., Dong, R., Espaillat, C., & Hartmann, L. 2012, *ApJ*, 755, 6

## APPENDIX

## A. DESCRIPTIONS OF INDIVIDUAL FAINT DISKS

A.1. *CHXR71*

CHXR71 is an M3 star (Luhman 2004; Manara et al. 2016) with an M5 secondary located at a projected separation of  $0.''56$ , or 100 AU (Lafrenière et al. 2008; Daemgen et al. 2013). In the optical spectrum, which is dominated by the primary component, the narrow and weak  $H\alpha$  line emission is consistent with chromospheric emission (Luhman 2004; Nguyen et al. 2012; Frasca et al. 2015). Fits to the UV continuum emission led to an accretion rate that is consistent with chromospheric activity (Manara et al. 2017). The warm dust near one of the stars produces at most a marginal excess at  $\lesssim 8 \mu\text{m}$  and a small excess at longer wavelengths, indicating substantial dust clearing within the innermost few AU of the disk.

A.2. *CHXR30A*

CHXR30A is a K7–K8 star (Luhman 2004; Manara et al. 2016) with a companion with a  $K_s$ -band contrast of 0.85 at a projected separation of  $0.''46$ , or 83 AU (Lafrenière et al. 2008). The  $K_s$  band contrast leads to an estimated mass ratio of  $\sim 0.4$ – $0.5$  in the Baraffe et al. (2015) models of pre-main sequence evolution, assuming that neither component has near-IR emission affected by a disk. Any accretion onto the primary is either very weak or undetected, with line emission that is consistent with chromospheric emission (Luhman 2004; Manara et al. 2017).

The SED of CHXR30A has a steep  $n_{2-13}$  index and a significant flux deficit at wavelengths  $\lesssim 8 \mu\text{m}$ , indicating that dust grains in the inner disk are largely depleted (Manoj et al. 2011). The continuum excess longward of  $13 \mu\text{m}$  is much fainter than that of typical Class II disks, though silicate features at  $10 \mu\text{m}$  and  $20 \mu\text{m}$  have moderate strengths that are comparable to Class II disks. The decreasing trend in flux towards longer wavelengths in the Spitzer-IRS spectrum ( $13$ – $31 \mu\text{m}$ , Manoj et al. 2011) differs significantly from the opposite trend commonly seen in transition disks (Calvet et al. 2005; Espaillat et al. 2007), which means that any inner dust wall is not prominent.

A.3. *T54*

T54 is a K0 star (Manara et al. 2016) with a K7 secondary at a projected separation of  $0.''24$ , or 43 AU (Daemgen et al. 2013). Based on a weak UV continuum excess, Manara et al. (2016) reported a low accretion luminosity, comparable to chromospheric noise. Espaillat et al. (2017) carefully investigated accretion properties of this target from  $H_2$ ,  $\text{Br}\gamma$ , He I, and  $H\alpha$  line emission and concluded that it is at most barely accreting.

Furlan et al. (2009) and Kim et al. (2009) classified T54 as a transition disk candidate because the IR SED is photospheric at wavelengths  $< 10 \mu\text{m}$  and rises longward of  $15 \mu\text{m}$ . The  $10 \mu\text{m}$  silicate feature is below the detection limits but PAH emission at  $11.3 \mu\text{m}$  is prominent (Espaillat et al. 2017). Far-IR excess ( $\lambda > 70 \mu\text{m}$ ) from *Herschel* photometry is largely contaminated by a nearby unidentified source (Matrà et al. 2012). Based on low dust mass and gas detection in the inner disk, Espaillat et al. (2017) argue that T54 is a young debris disk.

A.4. *CHXR20*

CHXR20 is a K6 star (Luhman 2004; Manara et al. 2017) with a wide companion separated by  $28.''46$  (Kraus & Hillenbrand 2007) and no known close companion from either high-resolution spectroscopy



(Nguyen et al. 2012) or Adaptive Optics imaging (Lafrenière et al. 2008). The star is weakly accreting, at a rate of  $1.95 \times 10^{-9} M_{\odot} \text{ yr}^{-1}$  as measured from the UV excess (Manara et al. 2017). Weak accretion is consistent with past measurements of  $H\alpha$  emission, which has an equivalent width consistent with a chromospheric origin (Luhman 2004; Frasca et al. 2015) but is also broad (Sacco et al. 2017) and includes absorption components in at least some epochs. The SED of CHXR20 shows a deficit of near-IR excess shortward of  $6 \mu\text{m}$ , similar to transitional disks, while the spectral slope at longer wavelength does not rise, as expected if the disk had a puffed-up wall typical of many transition disks (Espaillat et al. 2007). The mid-IR excess is fainter than typical Class II disks but is slightly brighter than that for CHXR71 and CHXR30A.

### A.5. ISO91

ISO91 is an M3 star with high extinction of  $A_J = 4.51$ , unlike most known members in Cha I (Luhman 2007). Due to its high extinction, information on multiplicity is not available. Accretion diagnostics from  $H\alpha$  or other measurements are also not available (Manara et al. 2017). After correction for extinction, the IR SED is similar to typical Class II disks, though with average lower IR excess. The  $10 \mu\text{m}$  and  $20 \mu\text{m}$  silicate emission is stronger than most other disks and than prediction from typical disk models (Manoj et al. 2011). Though continuum emission is only detected at  $3.8\sigma$  at source center, a large-scale  $^{12}\text{CO}$  outflow (see Figure 9) extends to  $\sim 10''$ , with centroid velocity consistent with the average system velocity for Chamaeleon I sample (Nguyen et al. 2012). The SED and mid-IR spectral slope appear disk-like (Dunham et al. 2015) and the source is not clearly detected with Herschel/PACS (Ribas et al. 2017). The outflow and extinction both indicate that ISO91 may still be embedded in an envelope and at an earlier stage of evolution than the other sources in this sample. Single-dish observations would help to reveal the presence of any envelope.

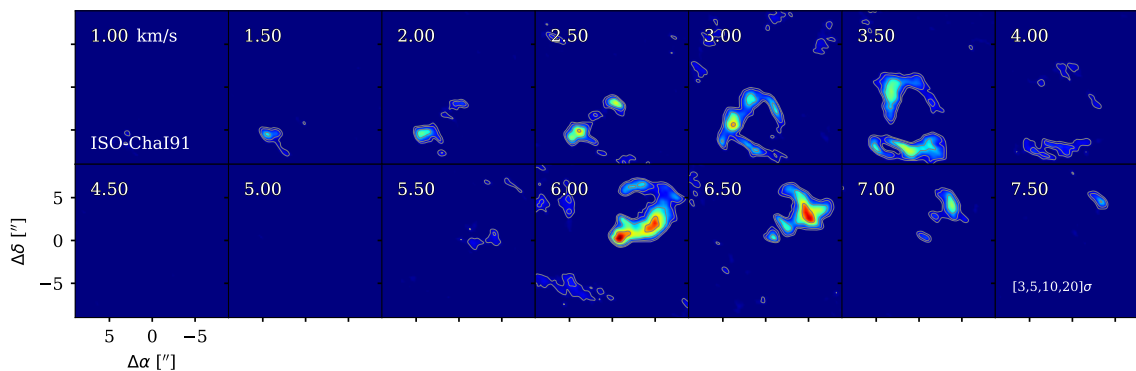


**Figure 9.** The  $^{12}\text{CO}$   $J = 3-2$  channel maps for ISO91, with channel velocity shown in the upper left corner. Large scale CO outflow extends to  $\sim 10''$ .

### A.6. T51

T51 is a K2 star with an M2 secondary (Manara et al. 2016) located at a projected separation of  $1.''9$  (Reipurth & Zinnecker 1993; Correia et al. 2006; Lafrenière et al. 2008). The binary was resolved in VLT/X-shooter observations, with measured accretion rates of both components comparable to typical Class II disks for each relevant spectral type (Manara et al. 2016). Most spectra of  $H\alpha$  confirm the presence of accretion,

with clear accretion signatures in line strength and line width (Wahhaj et al. 2010; Frasca et al. 2015). An initial non-detection of H $\alpha$  emission by Covino et al. (1997) may indicate that the presence of accretion is variable. The near-IR excess of T51 indicates an optically thick inner disk, again similar to typical Class II disks. However, the 13–31  $\mu$ m spectral index is particularly weak, which Furlan et al. (2009) and Manoj et al. (2011) explain as an outward truncation by the  $\sim 2''$  companion.

## B. SEDS FOR BRIGHTER SOURCES

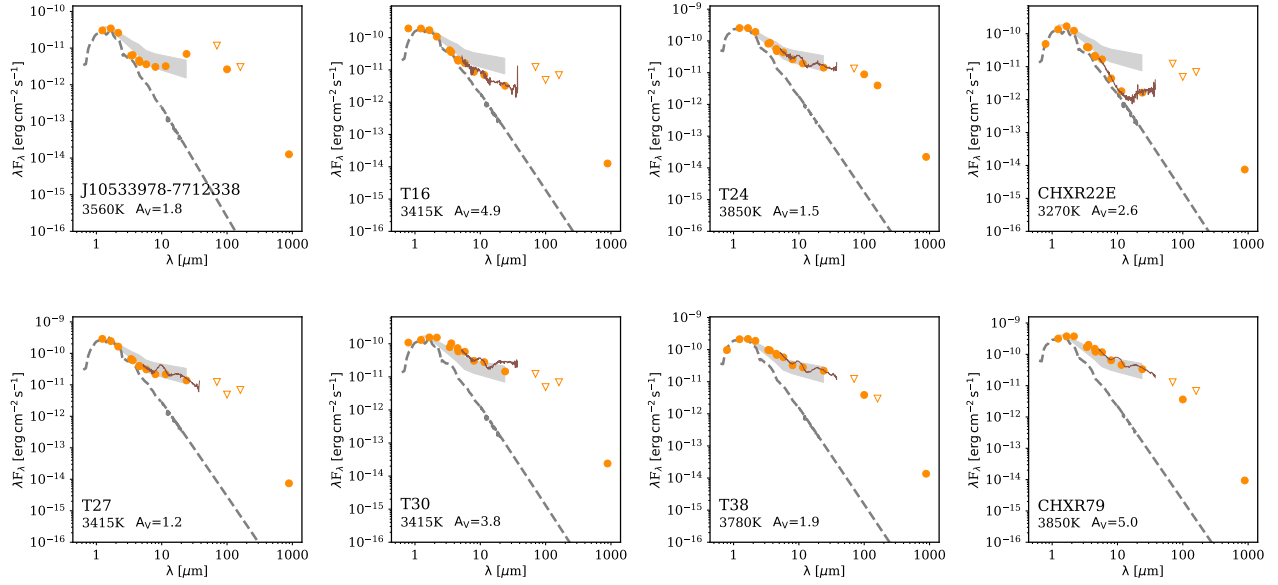


**Figure 10.** SEDs for the brighter sources in our ALMA Cycle 3 observation. Same as Figure 4.